Optical Pumping of Rubidium

Jonas Dej

Cavendish Laboratory, University of Cambridge, United Kingdom

(Dated: November 14, 2025)

In the quest to build scalable quantum computers, neutral-atom architectures based on rubidium are among the most promising platforms. In this work we characterise the two naturally occurring rubidium isotopes, ^{85}Rb and ^{87}Rb, using optical pumping between its hyperfine levels to probe Zeeman splittings, Rabi oscillations, and power broadening. The extracted nuclear spin are found to agree with theoretical expectations to within 1.5 %. In addition, we obtain strong evidence for two-photon excitation and qualitatively resolve the high-field Zeeman structure in the Breit–Rabi regime.

Introduction

In recent years, neutral-atom platforms have progressed rapidly. Experiments have demonstrated optical-tweezer arrays with more than 6,000 qubits [1], realised quantum simulations of two-dimensional superconductors [2], and achieved major advances in precision sensing [3, 4]. Rubidium remains a central atomic species in these systems due to its simple alkali structure and accessible optical transitions.

One of the essential tools is optical pumping, which creates controlled population imbalance using polarised resonant light. It underpins essential operations such as laser cooling, spin preparation, and high-contrast readout [5, 6]. In this work, we use optical pumping to study the two naturally occurring rubidium isotopes, ^{85}Rb and ^{87}Rb, and to investigate several fundamental atomic-physics effects relevant to coherent control in quantum technologies.

We first measure the linear Zeeman splitting to extract the hyperfine Landé factors, obtaining $g_F^{(85)} = 0.495(5)$ and $g_F^{(87)} = 0.330(4)$, both in agreement with theoretical expectations at the 1% level. We then explore transient dynamics, observing Rabi oscillations and studying the effect of detuning, with large data sets showing good qualitative agreement with the expected two-level behaviour.

To probe saturation effects, we measure the dependence of peak height and linewidth on the driving-field amplitude. The results follow the predicted power-broadening model, establishing laboratory linewidths of $\Gamma_0^{(85)} = 5700 \pm 300$ Hz and $\Gamma_0^{(87)} = 3400 \pm 200$ Hz. We also observe clear two-photon excitation peaks for both isotopes; Fourier analysis rules out harmonic artefacts, and the extracted power laws agree with the expected scaling, providing strong evidence for genuine two-photon transitions. An attempt to detect three-photon processes produced inconclusive results.

Finally, we qualitatively examine the high-field Zeeman regime, where multiple transition branches emerge. The observed pattern is consistent with optical pumping predominantly driven by σ^--polarised light.

All measurements were performed using the commercially available TeachSpin *Optical Pumping of Rubidium* apparatus [7]. Analysis code and supplementary plots are available on GitHub [1].

Theoretical background

Atomic levels of rubidium

Rubidium is an alkali metal with a single valence electron and ground state in the $5^2S_{1/2}$ manifold. The first excited manifold 5^2P is split by spin–orbit coupling into $5^2P_{1/2}$ and $5^2P_{3/2}$, and each fine-structure level is further divided into hyperfine sublevels by the interaction between the electron and nuclear spins (Fig. 1). Two stable isotopes occur naturally, ^{85}Rb and ^{87}Rb, with nuclear spins $I_{85} = 5/2$ and $I_{87} = 3/2$ and abundances of roughly 72% and 28% respectively [8]. In this experiment we address the $5^2S_{1/2} \rightarrow 5^2P_{1/2}$ transition at 794.8 nm [9].
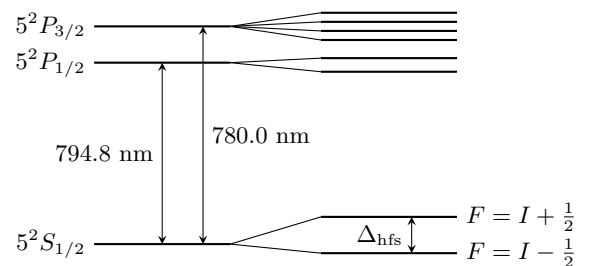

FIG. 1. Energy-level diagram of rubidium showing fine and hyperfine structure.

Zeeman splitting and Breit–Rabi regime

In the absence of a magnetic field, hyperfine states are labelled by the total angular momentum $F = I + J$ with a $(2F + 1)$-fold degeneracy in m_F. For weak magnetic fields, where the Zeeman interaction is small compared with the hyperfine splitting, the energy shift is linear in B [10],

$$\Delta E = g_F \mu_B m_F B, \tag{1}$$

---

with μ_B the Bohr magneton and g_F the hyperfine Landé factor. For $J = 1/2$ states,

$$g_F = \pm \frac{g_J}{2I + 1}, \qquad (2)$$

where $g_J \simeq 2.00232$ and the sign corresponds to $F = I \pm \frac{1}{2}$. For rubidium this gives $g_F^{(85)} \approx 0.3337$ and $g_F^{(87)} \approx 0.5006$, so the spacing between neighbouring Zeeman sublevels is approximately constant in the linear regime and directly proportional to B.

The relevant nuclear and hyperfine parameters are summarised in Table I. In stronger magnetic fields, the coupling between $\mathbf{I}$ and $\mathbf{J}$ is progressively broken, and the eigenstates evolve towards the uncoupled basis $|m_J, m_I\rangle$. As a result, the Zeeman shifts become nonlinear. This high-field behaviour is captured by the Breit-Rabi formula, which predicts a characteristic curvature and rearrangement of the level spacings. The full structure is shown in Fig. 2 for the $5^2S_{1/2}$ ground state of ^{87}Rb. Importantly, in this regime the spacing between neighbouring transitions is no longer constant, allowing individual transitions to be resolved without simultaneously driving all of them, as happens in the linear Zeeman regime.

TABLE I. Properties of naturally occurring rubidium isotopes [8, 9].

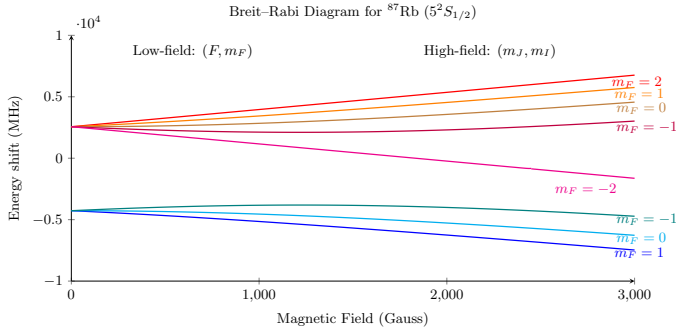| Isotope	Nuclear spin I	Landé factor g_F	Abundance (%)
^{85}Rb	5/2	0.5006	72
^{87}Rb	3/2	0.3337	28

FIG. 2. Zeeman splitting of the $5^2S_{1/2}$ ground state of ^{87}Rb in the Breit–Rabi regime, illustrating the transition from linear to nonlinear behaviour.

Optical pumping

The Zeeman splittings correspond to temperatures below a millikelvin, so at room temperature the Zeeman sublevels are thermally populated almost uniformly. To generate a population imbalance, we use optical pumping: resonant circularly polarised light drives allowed transitions until atoms accumulate in a state that is dark to the pump.

In our case, σ^--polarised light on the $5^2S_{1/2} \rightarrow 5^2P_{1/2}$ transition drives $\Delta m_F = -1$ transitions between hyperfine states $|S, F, m_F\rangle$. The extreme state $|S, F, m_F = -F\rangle$ cannot be excited further, as no state with $m_F = -F - 1$ exists in the excited manifold. Atoms therefore accumulate in this dark state, producing biased population distribution.

If an unpolarised RF magnetic field resonant with a Zeeman splitting is applied, it can drive transitions out of the dark state. The resulting change in transmitted light intensity directly probes the Zeeman spectrum. Throughout this report we use this mechanism to measure g_F, observe Rabi oscillations and study nonlinear excitation processes.

Transient effects and Rabi oscillations

The dynamics of optical pumping and RF excitation can be understood by modelling a pair of Zeeman sublevels as an effective two-level system driven by a classical oscillating field. Such a model leads to so called Rabi Oscillations [11]. Neglecting relaxation, the population of the upper state oscillates in time as

$$P_2(t) = \frac{\Omega^2}{\Omega^2 + \Delta^2} \sin^2\left(\frac{t}{2}\sqrt{\Omega^2 + \Delta^2}\right), \qquad (3)$$

where Δ is the detuning from resonance and Ω is the Rabi frequency,

$$\Omega = \frac{e\,\mathbf{E} \cdot \langle 1|\,\mathbf{r}\,|2\rangle}{\hbar}. \qquad (4)$$

Here $\mathbf{E}$ is the RF electric field amplitude (or, more generally, the driving field) and $\langle 1|\,\mathbf{r}\,|2\rangle$ the dipole matrix element between the two states.

In practice, collisions, field inhomogeneities and coupling to additional levels cause dephasing and relaxation. The ideal oscillations of Eq. (3) are then exponentially damped, and the coherence time can be linked to the linewidth of the corresponding resonance [12].

$$\tau \approx \frac{1}{\pi\Gamma} = \frac{1}{\pi\sqrt{\Gamma_0^2 + 2\Omega^2}} \qquad (5)$$

In our discussion, it is sufficient to note the general trend that a wider linewidth corresponds to a shorter coherence lifetime.

Peak spectroscopy and broadening mechanisms

At low drive intensity, each Zeeman transition appears as a Lorentzian resonance in the transmitted light [13],

$$I(\omega) = I_0 \frac{(\Gamma/2)^2}{(\omega - \omega_0)^2 + (\Gamma/2)^2}, \qquad (6)$$

with resonance frequency ω_0 and full width at half maximum (FWHM) Γ. The area under the curve is set by the transition strength, while Γ reflects the inverse coherence time.

2

As the RF power is increased, the peak height initially grows approximately linearly with the driving strength, but eventually saturates once the optical pumping and relaxation rates balance. The dependence is well described by

$$I \propto \frac{2\Omega^2}{\Gamma_0^2 + 2\Omega^2} \propto \frac{V^2}{V^2 + V_{\text{sat}}^2}, \tag{7}$$

where Γ_0 is the natural (relaxed) linewidth and Ω is the Rabi frequency, which is proportional to the applied RF amplitude V. At the same time the linewidth broadens according to the standard power-broadening relation,

$$\Gamma = \sqrt{\Gamma_0^2 + 2\Omega^2}. \tag{8}$$

Additional broadening arises from several mechanisms [14]: collisions with buffer gas atoms (collisional or pressure broadening), finite transit time of atoms through the interaction region, and spatial inhomogeneities of the static and RF magnetic fields. These effects contribute an extra inhomogeneous component to Γ but do not change the basic Lorentzian shape at moderate powers.

At sufficiently high driving strength, higher-order processes become observable [15]. In an n-photon transition, n RF photons are absorbed simultaneously to bridge the energy gap between two Zeeman levels. The corresponding signal scales approximately as I^n with RF intensity I and thus becomes visible only at high power. In this nonlinear regime the associated peaks are typically weaker and broader than the primary one-photon resonances.

Experimental setup

The apparatus is based on the TeachSpin *Optical Pumping of Rubidium OP1-B* kit and consists of a spectroscopy unit, magnetic-field coils, RF signal generators, detectors and a digital oscilloscope. A block diagram of the signal flow is shown in Fig. 3; detailed specifications of the commercial modules can be found in Ref. [7]. Here we summarise the elements most relevant for the measurements.
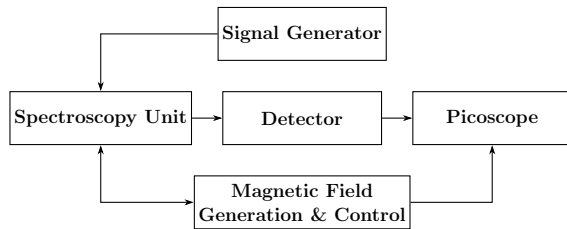

FIG. 3. Block diagram of the experimental setup.

Spectroscopy unit

The spectroscopy unit contains the rubidium discharge lamp, optical elements and heated absorption cell (Fig. 4). The discharge lamp consists of a gas bulb with rubidium metal and buffer gas inside an oven. An RF oscillator excites the gas, and radiative relaxation of the atoms produces resonance light at $780\,\text{nm}$ and $795\,\text{nm}$. An interference filter removes the $780\,\text{nm}$ component so that only light resonant with the $5^2S_{1/2} \to 5^2P_{1/2}$ transition enters the cell.
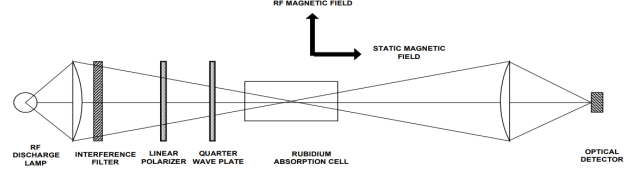

FIG. 4. Optical pumping apparatus (lamp, optics and heated rubidium cell).

The beam is circularly polarised and sent through a sealed vapor cell containing rubidium and a buffer gas (He or Ne) to reduce depolarising collisions with the walls. A static magnetic field is applied along the optical axis, and a transverse RF field is used to drive Zeeman transitions. The transmitted light is monitored by a photodiode. To suppress ambient light, the entire optical assembly was covered with an opaque blanket during data taking.

Magnetic field control

Three orthogonal Helmholtz coil pairs generate controlled magnetic fields along the vertical, horizontal and sweep directions. Approximate calibrations are given in Table II. The design of Hemholtz coils ensured the field is homogeneous throughout the vapour cell up to deviation $\approx \left(\frac{x}{R}\right)^4 < 0.2\%$.

TABLE II. Approximate magnetic field calibration for each Helmholtz coil pair.

Coil Pair	Mean Radius (cm)	Turns per Side	Field per Current (G/A)
Vertical	11.7(1)	20	1.54(1)
Horizontal	15.8(2)	154	8.8(1)
Sweep	16.4(2)	11	0.603(7)

The coil currents are set by precision current drivers in which the reference voltage directly determines the current, ensuring stable and reproducible fields. A sensing resistor defines the effective circuit resistance, so the magnetic field can be inferred from the measured voltage across it. The field direction is reversed simply by swapping the coil polarity.

The vertical coil is used to cancel the Earth's field, the horizontal coil provides the static field along the optical axis, and the sweep coil adds a small time-dependent component for scanning Zeeman resonances. The sensing resistors are 1.0 Ω (vertical and horizontal) and 0.5 Ω (sweep), each with 1% uncertainty.

The sweep coil is driven by a voltage ramp combining start-field, sweep, and optional modulation signals. The sweep range extends to about 1.0 V ($\approx$1 A) with adjustable sweep times from 1 s to 1000 s, allowing both single and continuous scans.

Signal generators

RF photons were generated by a *HAMEG HM8130* signal generator [16] with frequency range up to 10 MHz and fine control of frequency and amplitude. The output was connected to the spectroscopy unit via a fixed 75 Ω coaxial cable. At the low frequencies used here $\lesssim$ 300 kHz impedance mismatch between 50 Ω output impedance and the cable was negligible, as verified by direct measurements of the delivered voltage.

For transient measurements a second generator (*TTi TG315*) provided trigger pulses to gate the HAMEG output. Its exact amplitude and harmonic content were not critical, since it was only used as a timing reference.

Detector and readout

The transmitted light was detected by a silicon photodiode with an integrated preamplifier. An additional amplifier stage removed the large DC offset and provided a variable gain up to approximately 10^3, followed by a two-pole low-pass filter with selectable time constants up to a 3 s. For slow, high-SNR sweeps the largest time constant was used, while fast transient measurements used the minimum setting.

Waveforms were recorded with a *PicoScope 2205A* [17] digital oscilloscope (bandwidth 25 MHz, sampling rate up to 200 MS/s). Data were exported as `.csv` files and analysed in `Python`; the analysis scripts are publicly available on GitHub.[2]

Results and discussion

Observed peaks

A typical spectroscopic trace is shown in Fig. 5. Five peaks are visible: a broad central feature at zero magnetic field and four symmetric side peaks.

At $B = 0$ the Zeeman splitting vanishes and the magnetic sublevels become degenerate, so optical pumping cannot establish a population difference. Absorption therefore increases, giving the central maximum. The four side peaks occur at non-zero B where optical pumping creates a dark state and RF excitation repopulates absorbing levels. The outer pair originates from ^{85}Rb and the inner pair from ^{87}Rb, as confirmed by the g_F values extracted in the next subsection. The left–right symmetry reflects the fact that the observable depends only on $|B|$.
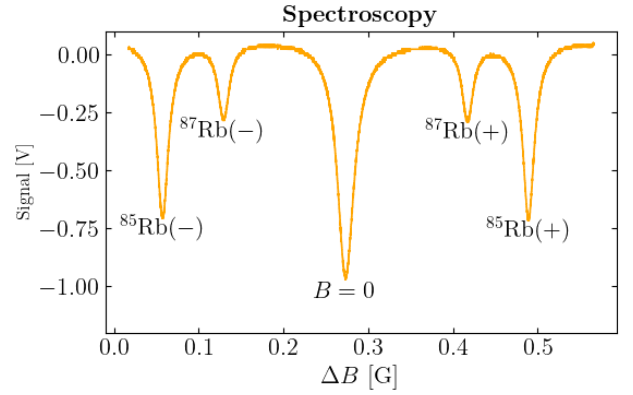
---

[2] `https://github.com/bullet-with-butterfly-wings/pumping.git`

FIG. 5. Typical spectroscopy signal of the rubidium vapor cell as the magnetic field is swept through zero.

Compensation of Earth's magnetic field

Accurate determination of the applied magnetic field requires compensation of the local geomagnetic field. The vertical component was cancelled by adjusting the vertical coil current to minimise the observed linewidths, as residual fields broaden the peaks. The horizontal component was reduced by rotating the entire setup so that the coil-generated field opposed the Earth's field; again the minimum in the linewidth provided the optimum setting, which was cross-checked with a compass application.

From the compensation currents we infer

$$
\begin{aligned}
B_x &= (0.28 \pm 0.02)\,\text{G}, \\
B_y &= (-0.36 \pm 0.07)\,\text{G},
\end{aligned}
\tag{9}
$$

corresponding to a total field $|B| = (0.46 \pm 0.06)\,\text{G}$ directed downwards with inclination $\theta = (52 \pm 6)°$. For Cambridge, typical values are 0.4–0.6 G and $\theta \approx 66°$ [18], so the measured field is consistent with partial shielding by the building.

Low-field Zeeman splitting and g_F factors

With the Earth's field compensated, we recorded Zeeman resonances over the full range of the sweep coil. From the sweep voltage, calibrated sweep time and coil parameters we extracted the magnetic field at each resonance. The dominant uncertainty in B comes from the reference resistors and coil dimensions, giving a combined systematic error of about 1.5%; the frequency uncertainty is below 0.1%. The magnetic field was swept over the full available range, corresponding to a measured voltage span of 0.995(2) V and a nominal sweep time of T = 10 s. However, from the signal observed on the Picoscope, the actual sweep time was determined to be T = 10.42(5) s. Therefore, both time and voltage range of the sweep were determined with resolution < 0.5%.

Figure 6 shows the measured resonance frequency as a function of B for all four observable transitions. The

data are very well described by straight lines, as expected from the linear Zeeman relation in Eq. (2). The slopes a of the fits determine the effective Landé factors via

$$g_F = \frac{ah}{\mu_B},\qquad(10)$$

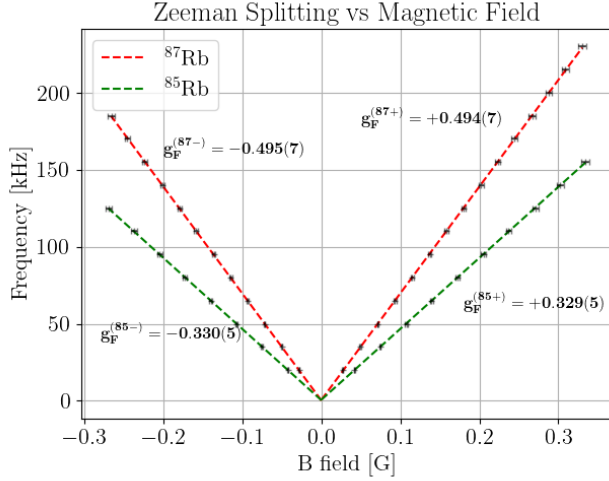and the fitted parameters are listed in Table III.

FIG. 6. Resonant frequency versus applied magnetic field for the four observed Zeeman transitions. Lines show linear fits.

TABLE III. Fit parameters of $f = aB + b$ for different spectroscopic peaks.

Peak	a (kHz/G)	b (kHz)	Δa	Δb	g_F
^{87}Rb $(+)$	692.03	0.658	1.34	0.27	0.494(7)
^{87}Rb $(-)$	-693.34	0.115	1.37	0.23	-0.495(7)
^{85}Rb $(+)$	460.45	0.706	0.83	0.17	0.329(5)
^{85}Rb $(-)$	-461.78	0.291	0.69	0.12	-0.330(5)

All four g_F values are slightly smaller in magnitude than the theoretical predictions, and the positive-frequency peaks show a somewhat larger intercept, likely due to a small residual uncompensated field. Nevertheless, the agreement is better than 1.5%.

Rabi oscillations

We next turned to the time-domain dynamics described in the theoretical section. With the RF drive pulsed at 10 Hz and the frequency set to 90 kHz, the system had time to repolarise into the optically pumped dark state between pulses. Each pulse then produced a transient modulation of the transmitted light, corresponding to Rabi oscillations between two Zeeman sublevels Fig. 7.

For each RF voltage, we recorded and averaged 64 time traces and fitted the resulting waveform with a damped version of Eq. (3), extracting the oscillation frequency,
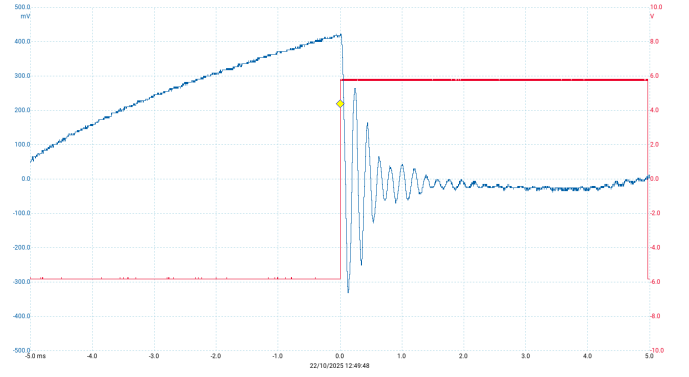

FIG. 7. Illustration of Rabi oscillations: coherent exchange of population between the optically pumped dark state and a coupled Zeeman sublevel.

amplitude and decay time. A small 50 Hz pickup, likely from the amplifier, limited the analysis to the first few oscillation cycles, where the background was approximately constant.

Figure 8 shows the fitted Rabi frequencies for both isotopes as a function of the applied RF voltage. The data follow the expected approximately linear dependence at small detuning, with a slight curvature near the origin attributable to residual detuning. The slope is significantly larger for ^{87}Rb than for ^{85}Rb,

$$\frac{\text{slope}_{87}}{\text{slope}_{85}} \approx 1.4 \approx \frac{g_F^{(87)}}{g_F^{(85)}},$$

consistent with the dependence of Ω on the matrix element in Eq. (4) and on the hyperfine structure.
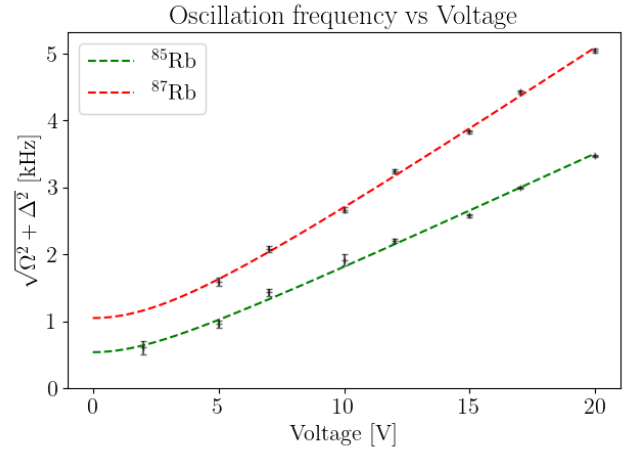

FIG. 8. Rabi frequency versus RF drive voltage for both rubidium isotopes.

The oscillation amplitude, shown in Fig. 9, initially increases with drive strength and then saturates, as expected for a two-level system driven close to resonance.

While noise and limited time resolution prevent a detailed comparison with the ideal model, the overall behaviour agrees well with the qualitative expectations. The decay times were found to increase with the applied voltage by roughly 30%. In all cases, ^{87}Rb exhibited longer lifetimes than ^{85}Rb, consistent with the differences in level structure and dephasing mechanisms. However, significant background noise led to a wide spread in the extracted decay constants for each driving amplitude, making a detailed quantitative analysis difficult.
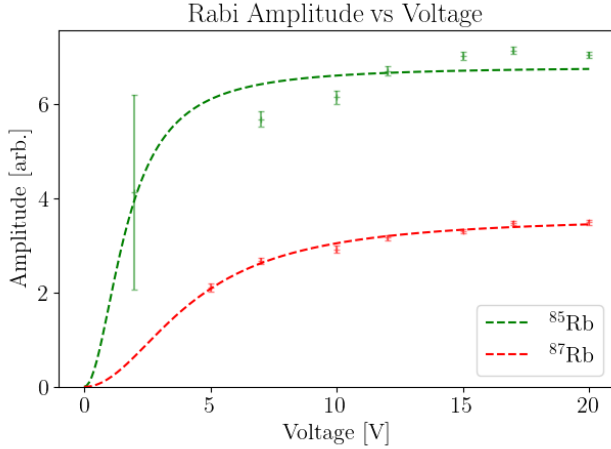

FIG. 9. Oscillation amplitude versus RF drive voltage for both isotopes.

Detuning effects were probed by fixing the RF amplitude at $20\,\mathrm{V}$ and scanning the frequency around the resonance of the ^{87}Rb peak. The resulting dependence of the oscillation frequency and amplitude on detuning qualitatively follows the envelopes predicted by Eq. (3), although simple two-level fits exhibit a systematic frequency offset. An empirical model including a small additive offset produces a significantly improved χ^2, suggesting additional multilevel or systematic contributions beyond the ideal two-level description. The extracted Rabi frequencies are broadly consistent with the estimates obtained from Fig. 8.

Power broadening and peak height

We now examine how the steady-state resonance peaks depend on the RF power. Spectra were recorded for drive voltages between $25\,\mathrm{mV}$ and $20\,\mathrm{V}$, covering almost three orders of magnitude. Each peak was fitted with a Lorentzian profile (with an added linear background at the weakest drives) to extract its height and width.

A modulation frequency of $150\,\mathrm{kHz}$ was used so that other features appeared as an approximately constant offset. The nominal sweep time was $50\,\mathrm{s}$, but for the smallest peaks slow time-dependent voltage drift was observed; in those cases we used a shorter $20\,\mathrm{s}$ sweep to minimise accumulated error. For all measurements, a $3\,\mathrm{s}$
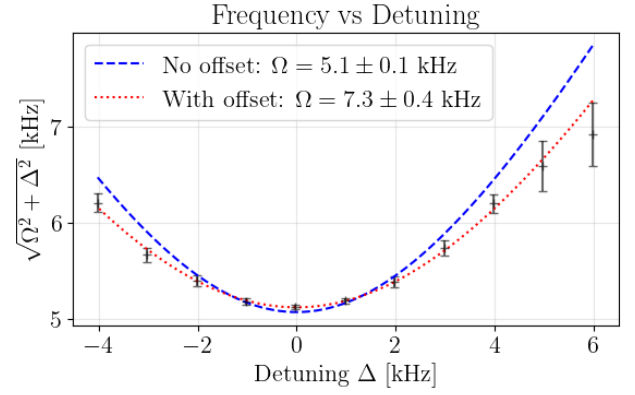

FIG. 10. Oscillation frequency as a function of detuning. The quoted uncertainties are statistical.
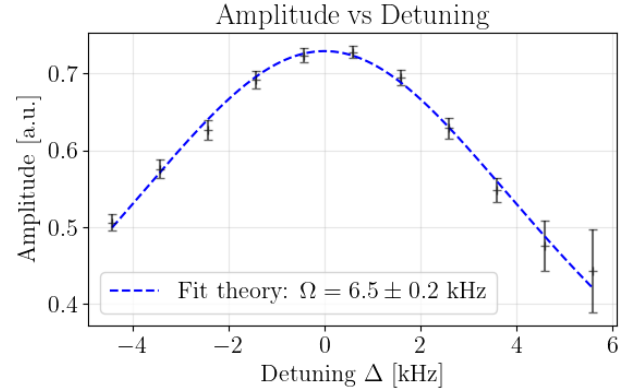

FIG. 11. Oscillation amplitude as a function of detuning. The overall behaviour is in good agreement with the expected envelope.

time constant was chosen to ensure a high SNR.

Conversion between sweep voltage and frequency relied on the calibrated coil parameters; the uncertainty results are summarised in Table IV. The total uncertainty in the linewidth is about 5%.

Figure 12 shows the peak height as a function of drive amplitude. Both isotopes exhibit the expected saturation behaviour: a roughly linear rise at low power, followed by a clear flattening above $V_{\mathrm{drive}} \sim 1\,\mathrm{V}$. The fit curves (dashed lines) use a simple saturation model motivated by Eq. (7) and the balance between pumping and relaxation.

The corresponding linewidths are plotted in Fig. 13. Both isotopes show a clear increase of Γ with drive amplitude, in qualitative agreement with the power broadening expression (8). Throughout the range, the ^{85}Rb resonance remains broader as the ^{87}Rb line, reflecting the larger number of Zeeman sublevels and stronger inhomogeneous dephasing in the $I = 5/2$ manifold. A summary
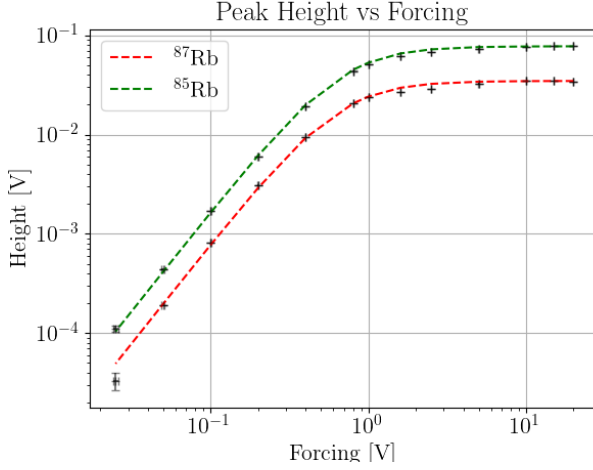
FIG. 12. Peak height versus RF drive amplitude for the ^{85}Rb and ^{87}Rb hyperfine resonances at 150 kHz. Dashed lines show fits to a saturation model based on the discussion in Sec. .

of the fitted linewidth parameters is given in Table IV.
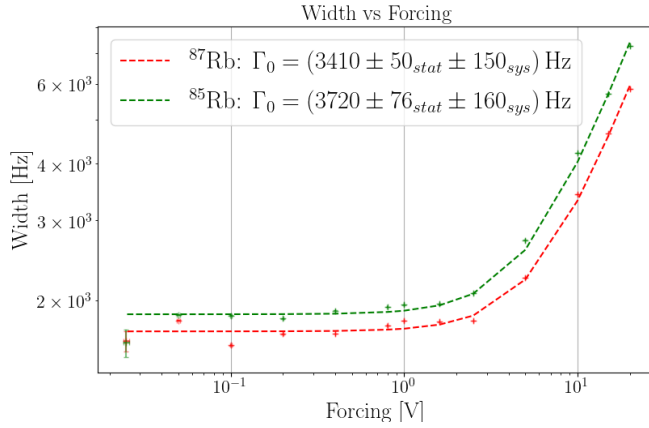

FIG. 13. Measured linewidth of the hyperfine resonances versus RF drive amplitude.

TABLE IV. Fitted linewidth parameters at 150 kHz drive frequency. Statistical and systematic uncertainties are quoted separately.

Isotope	Γ_0 [Hz]	$\Delta\Gamma_{stat}$ [Hz]	$\Delta\Gamma_{sys}$ [Hz]	$\Delta\Gamma_{tot}$ [Hz]
^{87}Rb	3410	50	150	158
^{85}Rb	3720	76	160	177

Multiphoton peaks

To explore the nonlinear regime, we searched for two- and three-photon excitation peaks. After locating a one-photon resonance at $f_{RF} = 200$ kHz, the RF frequency was halved so that any remaining signal at the same magnetic field must arise from absorption of two photons. Because these peaks are intrinsically weak, it was

crucial to distinguish genuine multiphoton signals from artefacts due to higher harmonics in the RF chain. A Fourier analysis of the RF waveform was therefore used to estimate the contribution from parasitic harmonics, which was then converted into an upper bound on the corresponding single-photon peak height using the saturation curve in Fig. 12.

Figure 14 shows the resulting peak heights as a function of RF amplitude for both isotopes, together with the estimated harmonic background. In both cases the observed peaks lie well above this background and follow a power law $H \propto V^\alpha$ with exponents

$$\alpha_{85} = 4.0 \pm 0.1, \qquad \alpha_{87} = 3.1 \pm 0.6,$$

compatible with the expected quartic scaling of a two-photon transition.
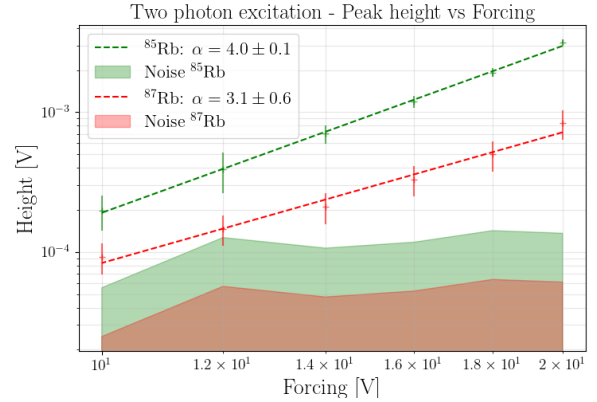

FIG. 14. Two-photon excitation peaks for both isotopes. The data lie clearly above the estimated contribution from RF anharmonicity, and the extracted power-law exponents are consistent with two-photon processes.

An analogous attempt was made to observe three-photon excitation by tuning the ^{85}Rb resonance to 300 kHz and then measuring at one third of that frequency. Here the expected three-photon signal overlaps with the two-photon transition of ^{87}Rb, and several data points fall below the estimated harmonic noise floor (Fig. 15). The fitted exponent $\alpha = 6.0 \pm 1.0$ is broadly compatible with the expected sixth-order scaling, but the evidence is not sufficient to claim an unambiguous observation of a genuine three-photon transition.

High-field Zeeman structure

Finally, we qualitatively explored the high-field regime where the Breit–Rabi nonlinearities become important. As the static field and RF frequency were increased, each low-field Zeeman peak gradually split into multiple components, as shown in Figs. 16 and 17. Longer sweep times correspond to higher fields.

For ^{85}Rb ($I = 5/2$), the ground state splits into the $F = 3$ and $F = 2$ manifolds, which evolve towards the
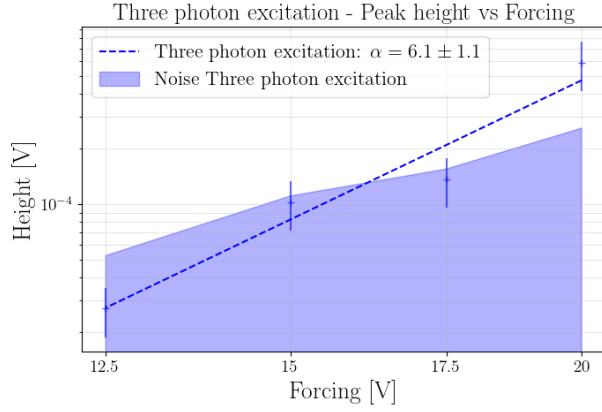
FIG. 15. Attempt to observe three-photon excitation. A subset of points lies below the estimated anharmonicity background, so the result is suggestive but not conclusive.
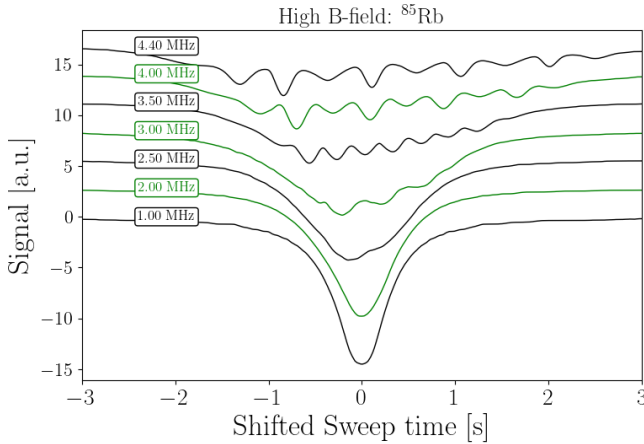

FIG. 17. Evolution of the ^{87}Rb resonance with increasing static field.

FIG. 16. Evolution of the ^{85}Rb resonance with increasing static field. Multiple components appear as the system enters the Breit–Rabi regime.

uncoupled $|m_J, m_I\rangle$ basis in the high-field limit. The Breit–Rabi model predicts ten allowed $\Delta m_J = \pm 1$ transitions: six originating from $F = 3$ and four from $F = 2$, appearing in an alternating sequence. In Fig. 16 we indeed observe a set of peaks with alternating strengths, consistent with this structure. The relative intensities indicate that predominantly σ^- pumping drives population towards the lowest m_F states, making the $F = 2$ lines comparatively stronger.

For ^{87}Rb ($I = 3/2$), a similar argument yields six allowed transitions at high field, arising from the $F = 2$ and $F = 1$ manifolds. The measured spectrum in Fig. 17 displays exactly six components with alternating strengths. Although the magnetic-field calibration was not precise enough for a quantitative comparison, the observed splitting pattern matches the qualitative structure expected from the Breit–Rabi diagram in Fig. 2.
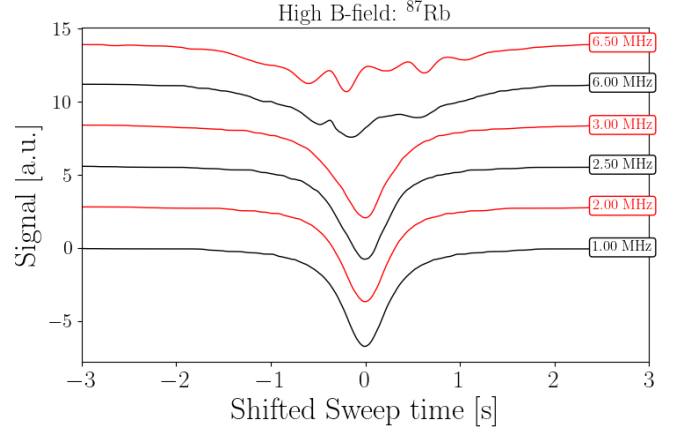
Conclusion

Using a commercial optical-pumping apparatus, we have characterised the Zeeman structure and driven dynamics of rubidium vapour. Low-field measurements yielded Landé g_F factors for both isotopes in percent-level agreement with the hyperfine model. In the time domain, we observed Rabi oscillations with the expected dependence on RF amplitude and detuning, while steady-state spectra showed clear saturation and power broadening. At high RF power, two-photon excitation peaks with the expected quartic scaling were identified, and tentative evidence for three-photon processes was also obtained. Scans at large magnetic fields revealed the qualitative rearrangement of Zeeman components anticipated from the Breit–Rabi model.

Future work could include measuring the linewidth as a function of RF frequency, providing a direct comparison with the Rabi frequency, as well as a more quantitative study of the high-field regime and additional data to clarify the presence of three-photon excitation. Overall, the results demonstrate how a simple tabletop setup can access a wide range of linear and nonlinear light–matter interactions.

[1] P. Scholl, F. Schäfer, W. Williams, L. Lassablière, A. Fedorov, and A. Browaeys, Nature **622**, 723 (2023).
[2] D. K. Nabben, J. Puig, C. Sánchez, T. Weinelt, H. Schweinfurth, K. Ralf, and W. Zwierlein, Nature **621**, 276 (2023).
[3] M. A. Norcia, K. Dordevic, H.-S. Kim, and A. M. Kaufman, Science **383**, 1092 (2024).
[4] A. K. Pedersen, C. Printz, J. Christensen, J. Jersblad, and A. J. Hilliard, Nature **628**, 517 (2024).
[5] T. M. Graham, M. Kwon, *et al.*, Nature **604**, 457 (2022), optical pumping used to isolate cycling transitions for high-contrast readout.

[6] W. Happer, Reviews of Modern Physics **44**, 169 (1972).

[7] TeachSpin, Inc., *Optical Pumping of Rubidium (OP1-B) Instruction Manual*, TeachSpin, Inc., Buffalo, NY, USA (2017), available as part of the *Optical Pumping of Rubidium OP1-B* experimental kit.

[8] E. Browne and J. K. Tuli, Nuclear Data Sheets **122**, 293 (2014), evaluated Nuclear Structure Data File (ENSDF) for rubidium isotopes, Brookhaven National Laboratory.

[9] A. Kramida, Y. Ralchenko, J. Reader, and N. A. Team, NIST Atomic Spectra Database (ver. 5.11), `https://physics.nist.gov/asd` (2024), national Institute of Standards and Technology, Gaithersburg, MD.

[10] C. J. Foot, *Atomic Physics* (Oxford University Press, 2005).

[11] C. Cohen-Tannoudji, J. Dupont-Roc, and G. Grynberg, *Atom–Photon Interactions: Basic Processes and Applications* (Wiley, New York, 1998) comprehensive discussion of Rabi oscillations and dressed states.

[12] L. Allen and J. H. Eberly, *Optical Resonance and Two-Level Atoms* (Dover Publications, New York, 1987).

[13] M.-P.-I. für Quantenoptik, Saturation spectroscopy, `https://www.mpq.mpg.de/4992695/saturation_spectroscopy.pdf`, lecture notes, accessed 2025-02-14.

[14] W. Demtröder, *Laser Spectroscopy: Basic Concepts and Instrumentation*, 3rd ed. (Springer, 2003) comprehensive discussion of natural, Doppler, collisional, transit-time, and power broadening.

[15] R. W. Boyd, *Nonlinear Optics*, 3rd ed. (Academic Press, 2008) see Chap. 2–4 for multiphoton absorption and power-law scaling.

[16] HAMEG Instruments GmbH, *HAMEG HM8130 Function Generator User Manual*, Mainhausen, Germany (2008), available online at `http://donporco.free.fr/lamartine/upload/74908Hameg_HM8130.pdf`.

[17] Pico Technology, *PicoScope 2205A PC Oscilloscope User Manual* (2023), accessed 2025-02-14.

[18] British Geological Survey, Geomagnetic data and models, `https://www.geomag.bgs.ac.uk/` (2024), retrieved November 15, 2024.